Received: 5 December 2021 | Revised: 9 February 2022 | Accepted: 10 February 2022

DOI: 10.1002/bit.28063

ARTICLE

BIOTECHNOLOGY AND BIOENGINEERING WILEY

Process monitoring framework for cross-flow diafiltration-based virus-like particle disassembly: Tracing product properties and filtration performance

Nils Hillebrandt | Philipp Vormittag | Annabelle Dietrich | Jürgen Hubbuch

Institute of Engineering in Life Sciences, Section IV: Biomolecular Separation Engineering, Karlsruhe Institute of Technology (KIT), Karlsruhe, Baden-Württemberg, Germany

Correspondence
Jürgen Hubbuch, Institute of Engineering in Life Sciences, Section IV: Biomolecular Separation Engineering, Karlsruhe Institute of Technology (KIT), Fritz-Haber-Weg 2, 76131 Karlsruhe, Baden-Württemberg, Germany.
Email: juergen.hubbuch@kit.edu

Funding information
Deutsche Forschungsgemeinschaft, Grant/Award Number: 273937032

Abstract

Virus-like particles (VLPs) are an emerging biopharmaceutical modality with great potential as a platform technology. VLPs can be applied as gene therapy vectors and prophylactic or therapeutic vaccines. For non-enveloped VLPs, recombinant production of the protein subunits leads to intracellular self-assembly. The subsequent purification process includes VLP dis- and reassembly which aim at removing encapsulated impurities and improving particle properties. Filtration-based separation and processing has proven successful for VLPs but requires large product quantities and laborious experiments in early development stages. Both challenges can be tackled by implementation of process analytical technology (PAT) to efficiently obtain extensive process information. In this study, an existing PAT setup was extended to comprehensively monitor the diafiltration-based disassembly of hepatitis B core antigen (HBcAg) VLPs. Process-related signals were monitored in-line, while product-related signals, such as ultraviolet light (UV) spectra as well as static and dynamic light scattering (SLS and DLS), were monitored on-line. The applicability of the sensors for disassembly monitoring was evaluated under varying processing conditions. HBcAg VLP subunit concentrations were accurately predicted based on UV data using ordinary and partial least squares regression models (Q^2 from 0.909 to 0.976). DLS data were used for aggregation monitoring while the SLS intensity qualitatively reflected the disassembly progress.

KEYWORDS
cross-flow filtration, disassembly, downstream processing, process analytical technology, tangential flow filtration, virus-like particles

Abbreviations: A260/A280, absorbance ratio 260 to 280 nm; CFF, cross-flow filtration; CV, cross validation; DLS, dynamic light scattering; DV, diafiltration volumes; HBcAg, hepatitis B core antigen; HPLC, high-performance liquid chromatography; nLV, number of latent variables; OLS, ordinary least squares; PAT, process analytical technology; PLS, partial least squares; PRESS, predictive residual sum of squares; RMSE, root mean square error; RMSECV, root mean square error of cross validation; RMSEP, root mean square error of prediction; SEC, size-exclusion chromatography; SLS, static light scattering; UV, ultraviolet light; VLP, virus-like particle; *z*-average, *z*-average hydrodynamic particle diameter.

1 | INTRODUCTION

Virus-like particles (VLPs) are particulate assemblies of viral subunit proteins that lack the viral genome. This makes VLPs non-infectious and thus versatile biopharmaceuticals. VLPs usually resemble their originating virus and can therefore be applied as vaccines against the native virus. Among these, vaccines against hepatitis B (for instance, Recombivax HB by Merck & Co, Inc or Engerix-B by GlaxoSmithKline Biologicals), human papillomavirus (for instance, Gardasil by Merck & Co, Inc or Cervarix by GlaxoSmithKline Biologicals), or hepatitis E (Hecolin by Xiamen Innovax Biotech) are approved for human use. So-called chimeric VLPs contain a foreign peptide or epitope which is inserted into or fused to the protein subunit. Multiple chimeric VLP vaccine candidates were developed against infectious diseases such as malaria (Kingston et al., 2019; Rutgers et al., 1988), influenza A (Neirynck et al., 1999), coronavirus disease 2019 (COVID-19) (Chu et al., 2021; Tan et al., 2021; Yang et al., 2021; Zha et al., 2021), or choriomeningitis (Sedlik et al., 1997). The malaria vaccine RTS,S/AS01 (Chandramohan et al., 2021) is approved as Mosquirix by GlaxoSmithKline Biologicals and was recently recommended by the WHO (World Health Organization, 2021) for children living in countries with a certain malaria transmission. Furthermore, chimeric VLPs are potential prophylactic or therapeutic vaccines against various cancers (Kaufmann et al., 2007; Klamp et al., 2011; Palladini et al., 2018; Zhang et al., 2007). VLPs and chimeric VLPs are also applied as nanocarrier for therapeutic cargo such as nucleic acids, proteins, or chemical drugs (Ashley et al., 2011; Cerqueira et al., 2017; Hartzell et al., 2020; Petrovskis et al., 2021; Shan et al., 2018).

The spontaneous self-assembly of subunits into VLPs in the host cell (in vivo) may lead to malformed VLPs (Roldão et al., 2012) or encapsulated impurities (Mohsen et al., 2018; Strods et al., 2015; Vicente et al., 2011). The disassembly of these in vivo-assembled VLPs into subunits and the following reassembly have been shown to improve their homogeneity, stability, and immunogenicity (Zhao, Allen, et al., 2012; Zhao, Modis, et al., 2012). While dis- and reassembly are beneficial regarding the purity and structure of the VLPs, it also enables packaging of therapeutic cargo (Ashley et al., 2011; Cerqueira et al., 2017; Petrovskis et al., 2021; Shan et al., 2018). VLP disassembly is usually performed by changing the liquid phase conditions, namely pH, ionic strength, and the concentration of chaotropic or reducing agents (Ashley et al., 2011; Carreira et al., 2004; Hillebrandt et al., 2021; McCarthy et al., 1998). The change of the liquid phase conditions can be performed by dialysis at laboratory scale (Holmes et al., 2015; Strods et al., 2015) but at a larger scale more efficient processing by diafiltration (Phillips & Signs, 2004) is desirable. Cross-flow filtration (CFF), also known as tangential flow filtration (TFF), has proven as suitable downstream processing operation for virus and VLP processing (Carvalho et al., 2019; Grzenia et al., 2008; Hillebrandt et al., 2020; Kalbfuss et al., 2007; Liew et al., 2012; Lin et al., 2015; Moleirinho et al., 2018; Negrete et al., 2014; Peixoto et al., 2007; Wickramasinghe et al., 2005). Therefore, we recently implemented a diafiltration-based VLP disassembly process step that showed additional purification capabilities (Hillebrandt et al., 2021).

The efficiency and duration of the disassembly reaction mainly depend on the liquid phase conditions (Ausar et al., 2006; Hillebrandt et al., 2021; Mach et al., 2006; Mellado et al., 2009). Changes in the amino acid sequence, such as for chimeric variants, have also been shown to influence the VLP disassembly (Carreira et al., 2004; Hillebrandt et al., 2021; Schumacher et al., 2018). Furthermore, it is presumed that the encapsulation of nucleic acids impacts the stability of certain VLPs (Porterfield et al., 2010; van Rosmalen et al., 2018; Yuan & Parrish, 2001). Variations in the impurity profile, namely the nucleic acid content, can therefore affect the disassembly performance.

In the development and manufacturing stage of (bio-) pharmaceuticals, process analytical technology (PAT) is a valuable tool to obtain process knowledge or facilitate process control through monitoring to ultimately ensure a high product quality (US Department of Health and Human Services—Food and Drug Administration, 2004). Recently, PAT was implemented to monitor critical quality attributes during CFF processes of biopharmaceutical proteins (Rolinger et al., 2020; Wasalathanthri et al., 2020; West et al., 2021). In the case of VLP disassembly, PAT could reveal the effect of changing liquid phase conditions or impurity levels on diafiltration-based disassembly and provide a solution for a data-based endpoint detection. A previously developed monitoring setup for diafiltration-based VLP reassembly showed high accuracy and revealed detailed insights into the reassembly process (Rüdt et al., 2019). The implementation of a PAT setup for VLP disassembly could complement the knowledge gained with insights into the preceding process step and enable a combination of both technologies, potentially creating synergies.

This study thus implements a monitoring framework as a PAT tool for the VLP disassembly using on-line ultraviolet light (UV) and light scattering sensors. An existing setup was advanced by on-line display of static light scattering (SLS) and by diafiltration progress monitoring using conductivity and pH. Hepatitis B core antigen (HBcAg) VLPs were used as non-enveloped model VLPs which disassemble into homodimeric HBcAg subunits. They are widely used, especially as a platform for chimeric VLPs (Karpenko et al., 2000; Klamp et al., 2011; Zhang et al., 2007) and as a nanocarrier (Petrovskis et al., 2021; Shan et al., 2018; Strods et al., 2015). The capabilities of the PAT tool concerning the disassembly of in vivo-assembled VLPs were evaluated by variation of the process duration and liquid phase conditions such as impurity level or salt concentration. The data were further used to compare simple and more complex control strategies based on univariate and multivariate data. Multivariate data analysis was based on ordinary least squares (OLS) and partial least squares (PLS) regression models.

2 | MATERIALS AND METHODS

2.1 | Chemicals, buffers, and VLPs

The chemicals used in this study were obtained from Merck KGaA, unless otherwise stated. All buffers and solutions were prepared with ultrapure water (PURELAB Ultra, ELGA LabWater), their pH adjusted with 32% HCl or 4 M NaOH (SenTix62 pH electrode [WTW] and HI 3220 pH meter [Hanna Instruments]), and filtered with 0.2 µm-pore size cellulose acetate filters (VWR). The HBcAg protein used in this study, Cp149, was truncated at its C-terminus and thereby contained only the first 149 amino acids (Zlotnick et al., 1996). Cp149 was heterologously produced in *Escherichia coli* as previously described (Hillebrandt et al., 2020). The plasmid containing the Cp149 genes was kindly provided by Prof. Adam Zlotnick (Indiana University, USA). The downstream process consisted of lysis by sonication, capture by precipitation/re-dissolution, and purification by diafiltration and multimodal size-exclusion chromatography (SEC) as previously described (Hillebrandt et al., 2021). The final VLP feedstock for this study was stored at −20°C and contained 3.7 g L^{-1} Cp149 in feed buffer (50 mM Tris at pH 7.2). The Cp149 dimer (further referred to as "dimer") molecular weight and extinction coefficient at 280 nm were determined to be 34 kDa and 1.764 L g^{-1} cm^{-1}, respectively, both based on the amino acids sequence (Gasteiger et al., 2005). A disassembly buffer consisting of 50 mM Tris and 3 M urea at pH 8.5 was used as diafiltration buffer. The feedstock NaCl concentration was adjusted with a 50 mM Tris, 505 mM NaCl high-salt buffer at pH 7.2.

2.2 | Filtration and monitoring setup

Diafiltration experiments were performed using a KrosFlo Research KRIIi CFF unit with backpressure valve (Spectrum Labs). The CFF system was equipped with a stirred retentate reservoir (Sartorius Stedim Biotech GmbH) and a 10 kDa molecular weight cut-off, 88 cm^2 Ultracel Pellicon 3 membrane (Merck Millipore). Permeate flow rate control was implemented using a SLS-1500 liquid flow meter (Sensirion AG; note that SLS does not stand for static light scattering in this case) with feedback to the backpressure valve as previously described (Hillebrandt et al., 2020). The feed line contained a T-piece with a septum for at-line sampling (injection plug, Fresenius Kabi). A piping and instrumentation diagram of the monitoring setup is shown in Figure 1. It was based on a previously established setup (Rüdt et al., 2019) which was extended by several components. Besides the standard in-line pressure sensors, in-line pH and in-line conductivity sensors were implemented. In detail, a pH electrode including flow cell (product number: 18-1134-84; GE Healthcare) was connected to an HI 3220 pH meter (Hanna Instruments) and a conductivity flow cell (product number: 18-1111-05) including a pH/C-900 monitoring unit (GE Healthcare) which was connected to a NI USB-6008 data acquisition device (National Instruments). On-line monitoring was performed with a sample loop

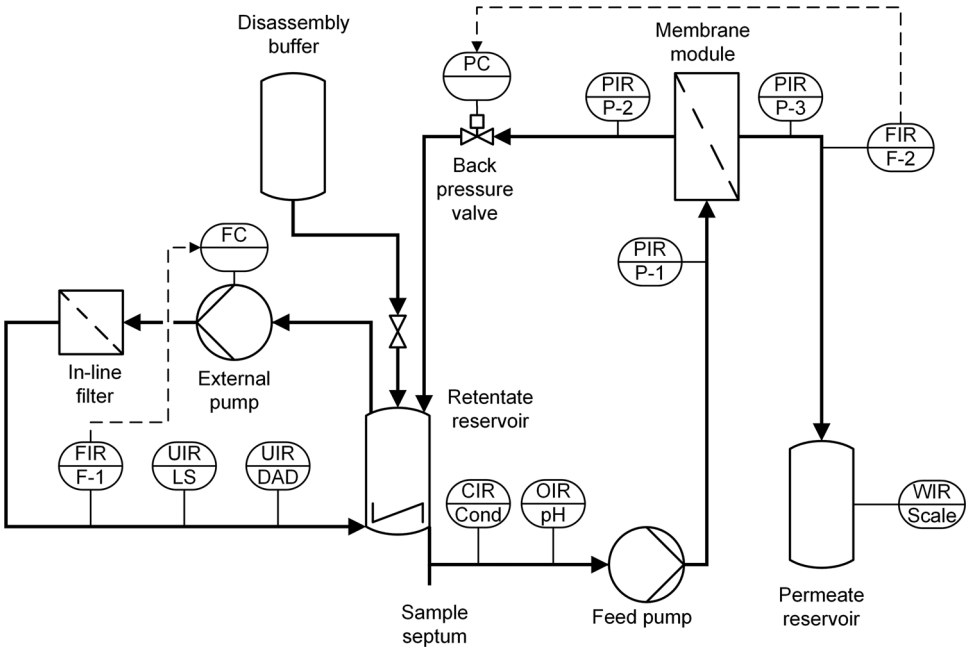

FIGURE 1 Piping and instrumentation diagram of the monitoring setup. All devices are connected to a personal computer (not shown to preserve clarity) with a graphical user interface that allows for the management of digital connections and settings. It further performs data management that includes recording and storage, supply of actuator controllers with sensor data, and real-time visualization of sensor data. Abbreviations: C (first letter) and Cond, conductivity; C (second letter), control; DAD, diode array detector; F, flow; I, indication; LS, light scattering; O, pH; P, pressure; R, recording; U, multivariable (spectrometry); W, weight

which was supplied with a constant flow rate setpoint of 1 mL min^{-1} using a Minipuls 3 peristaltic pump (Gilson). The flow rate measurement from a second SLS-1500 flow meter (Sensirion) was the input for an integral controller that controlled the pump speed via the data acquisition device to maintain the desired flow rate. A Minisart GF glass fiber filter (Sartorius Stedim Biotech GmbH) with 0.7 μm^2 pore size was used as a bubble and particle trap to enhance measurement performance. A Zetasizer Nano ZSP light scattering spectrometer (Malvern Instruments) with a 10 mm path length cuvette (Hellma Analytics) and a DAD-3000 RS diode array detector with a 0.4 mm path length flow cell (both Thermo Fisher Scientific) were implemented as sensors in the on-line loop. The elements of the on-line loop were connected by PEEK capillaries with an inner diameter of 0.75 mm whereas the last one in flow direction had an inner diameter of 0.25 mm to increase the backpressure and improve measurement quality.

2.3 | Diafiltration experiments

The disassembly was performed by constant volume diafiltration of 30 mL feed solution into disassembly buffer. The CFF feed and on-line loop flow rates were 30 and 1 mL min^{-1}, respectively. The feed conditions and further process parameters of the disassembly experiments are listed in Table 1. The Cp149 concentration was adjusted by dilution with feed buffer based on the 280 nm absorbance (NanoDrop 2000c; Thermo Fisher Scientific) and the Cp149 extinction coefficient. NaCl concentration and 260 to 280 nm absorbance ratio (A260/A280) were adjusted by dilution with high-salt buffer or less purified feed solution (post capture) instead of feed buffer. The feed solution was filtered by a 0.2 µm pore size cellulose acetate syringe filter (VWR). The CFF unit and the on-line loop were flushed with feed buffer before the experiment. A detailed description of the startup procedure can be found elsewhere (Rüdt et al., 2019). The membrane was cleaned according to the manufacturer's instructions between experiments. During diafiltration, 0.4 mL samples were taken at each diafiltration volume (DV), filtered by 0.22 µm pore size polyvinylidene fluoride Millex-GV filters (Merck Millipore), and analyzed by at-line SEC high-performance liquid chromatography (HPLC) as previously described (Hillebrandt et al., 2021). Briefly, the mobile phase was adapted to the composition of the analyzed sample, that is, the retentate buffer composition at the time of sampling, using mixtures of feed and disassembly buffer. SEC-HPLC concentrations were calculated from the peak areas using Beer's law.

2.4 | Data acquisition, processing, and analysis

All sensors and actuators of the experimental setup were connected to a computer running a custom-made MATLAB application with a graphical user interface (version R2019b; The Mathworks Inc.) that enabled central data collection, live visualization, and device control. The latter included the setting of a common time base, start/stop of acquisitions or actuations, integral control of the on-line loop pump, and data supply for the backpressure valve. The time alignment of the sensor data was performed by subtracting its delay time with respect to the retentate reservoir. DV were calculated from the permeate mass assuming a constant density of 1.045 g cm^{-3} and retentate volume of 30 mL. The dimer yield was calculated from the initial Cp149 and final dimer masses which were defined as the product of at-line SEC-HPLC concentrations and the process volume.

Light scattering data were acquired at 23°C and 173° backscatter in the Zetasizer's chromatography mode with a measurement duration (interval) of 10 s. Viscosities and refractive indices were assumed to be constant and set in the Zetasizer Software (version 7.12; Malvern Instruments) based on stored values for protein (sample) and the disassembly buffer composition (dispersant). The laser attenuation was adapted to aim for an SLS intensity in the range between 0.2×10^6 and 1.5×10^6 s^{-1} and corrected by attenuation factors according to the manufacturer's instructions. Smoothing of the recorded *z*-average hydrodynamic particle diameter (*z*-average) was performed by a moving median with a window of six data points (~1 min).

TABLE 1 Feed conditions and processing parameters of the monitored diafiltration-based disassembly experiments

Experiment	Cp149 conc. (g L^{-1})	Permeate flux (L m^{-2} h^{-1})	NaCl conc. (mM)	A260/A280 (-)	Duration (DV)	Set[a] (-)
Run 1	0.50	14	0	0.65	6	Cal.
Run 2	1.04	14	0	0.65	6	Val.
Run 3	2.06	14	0	0.65	6	Val.
Run 4	1.01	14	300	0.65	10 (6[b])	Cal.
Run 5	1.83	14	0	0.74	6	Cal.
Run 6	2.02	24	0	0.65	6	Cal.

[a]Classification into calibration set and external validation set for regression modeling.

Abbreviations: A260/A280, absorbance ratio 260 to 280 nm; cal., calibration; conc., concentration; DV, diafiltration volumes; val., validation.

[b]Regression model calibration was performed with data of the first 6 DV.

UV spectra were recorded in the wavelength range between 240 and 340 nm at a resolution of 1 nm and a frequency setpoint of 1 Hz. The on-line measured protein concentration was calculated from the 280 nm absorbance using Beer's law. The *a*/*b* ratio (Ragone et al., 1984) and the location of the minimum near 293 nm (tryptophan shift; Mach & Middaugh, 1994) were determined by second derivative spectroscopy of the recorded spectra. A detailed description of the procedure can be found elsewhere (Ausar et al., 2006; Rüdt et al., 2019).

2.5 | Regression modeling

Regression models were calibrated for the prediction of dimer concentrations from on-line UV data. PLS modeling was performed in MATLAB (version R2019b; The Mathworks Inc.) similarly as described by Großhans et al. (2018) but without any preprocessing. Briefly, the data of the first six DV of runs 1 and 4 to 6 (Table 1) were used for calibration by cross validation (CV) where each run represented one CV group. Repeatedly, one CV group was excluded and a PLS-1 regression (SIMPLS algorithm [de Jong, 1993], function *plsregress*) was performed with the remaining data until each group was excluded once. The predictive residual sum of squares (PRESS) was summed up over all iterations and scaled by the number of samples and number of latent variables (nLV) (Wold et al., 2001). The coefficient of determination R^2, the cross-validated coefficient of determination Q^2_{CV}, and the root mean square error of cross validation (RMSECV) were calculated according to Wold et al. (2001). Note that Q^2_{CV} and RMSECV were derived from the accumulated PRESS. The data of the remaining two runs 2 and 3 (Table 1) were used as external validation set. Details on the calculation of the coefficient of determination using the external validation data set Q^2_{Ext}, and the root mean square error of prediction (RMSEP) can be found in Nilsson et al. (1997) and Kessler (2006), respectively. The workflow for the OLS model was performed identically using two input variables resulting in a multiple linear model.

Before the calibration of the final PLS model, the nLV of the model was determined based on the Q^2_{CV}. Therefore, PLS models were calibrated for $1 \leq nLV \leq 9$. With increasing nLV, the first model which resulted in a local Q^2_{CV} maximum above 0.9 was selected. To further improve the PLS model, an additional variable selection was performed. Variable selection was optimized using a genetic algorithm (function *ga* for mixed integer optimization; Deep et al., 2009) with a population size of 500, similarly as suggested by Andersen and Bro (2010). The objective was to find a combination of wavelengths (input or X-variable of the PLS regression) that results in a minimal scaled PRESS after calibration by CV, as described above. During the optimization, the absorbance of each wavelength could either be included or omitted resulting in varying combinations of wavelengths generated by the genetic algorithm. For each combination, a PLS model was calibrated and the scaled PRESS calculated. Note that an additional UV data set of run 1 was recorded under identical conditions for regression model calibration as the initial set showed disturbances, which negatively affected the RMSECV.

3 | RESULTS AND DISCUSSION

A monitoring setup was implemented for the diafiltration-based disassembly of Cp149 VLPs which was performed under varying conditions as listed in Table 1. Briefly, runs 1–3 were performed at low, medium, and high protein concentration. The feed solution of run 4 had an elevated salt concentration while run 5 had an elevated impurity level and protein concentration. Run 6 was performed at a high protein concentration with a high permeate flux to expose Cp149 to elevated concentrations at the membrane surface and to reduce the processing time. Pressures, conductivity, and pH were monitored in-line while light scattering and UV spectroscopy were monitored on-line. Light scattering spectroscopy allowed for determination of the SLS intensity and the dynamic light scattering (DLS) *z*-average. UV spectroscopy (240–340 nm) allowed for determination of an on-line measured protein concentration and A260/A280 as well as for performing second derivative spectroscopy and regression modeling. As a reference, at-line SEC-HPLC was used to determine the concentrations of Cp149 dimers and high-molecular weight species such as Cp149 VLPs and potential aggregates. A detailed investigation of the influence of the conditions on the dimer yield was out of scope of this study. Yields were approximately between 0.7 and 0.8 (no scatter correction applied).

3.1 | At-line monitoring

At-line SEC-HPLC analysis was performed as the disassembly reaction was expected to be time-dependent (Hillebrandt et al., 2021) and the bias due to continuation of the disassembly reaction after sampling should be minimized. The results are shown in Figure 2 (top row). Generally, the dimer concentration increases over time and flattens out toward the end indicating the progress and final stage of the disassembly reaction, respectively. At the beginning of each run, higher dimer concentrations were detected for higher total Cp149 concentrations showing that a fraction of the VLPs was already partly disassembled under the given feed conditions. An exception is run 4 with a feed NaCl concentration of 300 mM, which resulted in the lowest initial dimer concentration followed by a lag phase before its increase. This lag phase can be attributed to the presence of NaCl which is mostly depleted during the first few DV. This matter is further discussed in detail in Section 3.3. All runs reached a dimer concentration plateau which was arbitrarily defined by a slope $\leq 0.0013\ g\ L^{-1} min^{-1}$. The beginning of each plateau is also highlighted in Figure 2. Except for run 1, the plateau was reached after 4–5 DV (fifth to sixth data point, samples were taken at each DV from 0 to 6). For run 1, the lower feed concentration was most probably the reason for an earlier decrease of the slope below the threshold.

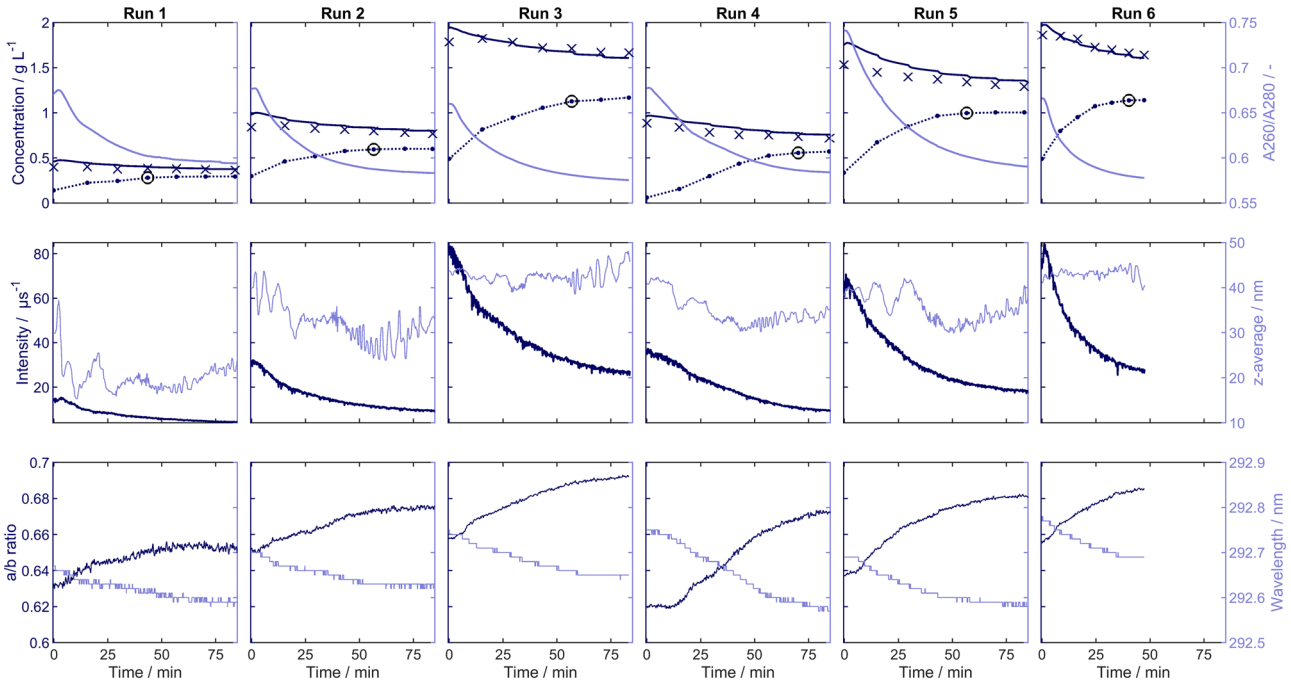

FIGURE 2 Process data from on-line monitoring. Each column represents the data of one experiment (compare Table 1). Top row: dimer concentration (dark blue dots with dotted lines to guide the eye and the beginning of the concentration plateau indicated by a black circle) and total Cp149 concentration (dark blue crosses) determined by at-line SEC-HPLC, on-line protein concentration (dark blue lines), and on-line A260/A280 (light blue lines). Center row: on-line SLS intensity (dark blue) and on-line *z*-average diameter from DLS measurements (light blue). The earlier was corrected by the laser attenuation factor according to the manufacturer's instructions and the latter was smoothed by a moving median with a window of six data points (~ 1 min). Bottom row: *a*/*b* ratio (dark blue) and wavelength minimum around 293 nm (light blue), both derived from second derivative spectroscopy. Axis limits were kept constant for all runs to enhance comparability. Another representation can be found in the Figure S1. Abbreviations: A260/A280, absorbance ratio 260to280 nm; DLS, dynamic light scattering; HPLC, high-performance liquid chromatography; SEC, size-exclusion chromatography; SLS, static light scattering

As an example, run 4 was continued until 10 DV (Figure S1) and the dimer concentration decreased slightly during the additional 4 DV. An explanation for this decrease is the sampling for at-line analysis and the resulting replacement of the sample volume by diafiltration buffer which leads to a minimal dilution of the dimers. During the disassembly reaction, this concentration reduction is superimposed by the formation of dimers.

Run 6 was performed under the same conditions as run 3 but with a higher permeate flux leading to a 36 min processing time reduction. Nevertheless, both processes show a similar progression of the dimer concentration on a DV basis (cf. Figure S1). In the investigated time frame and under the given conditions, the disassembly progress seems to depend mainly on the degree of buffer exchange rather than on process time. This observation was also made during the reassembly process (Rüdt et al., 2019) but is in contrast to the observed time-dependence of small scale batch disassembly reactions (Hillebrandt et al., 2021). An explanation for this observation could be that intensified mixing and shear stress during the filtration process accelerate the disassembly reaction. However, these observations and assumptions should be verified in further studies. Overall, the variation of processing parameters as well as the variability in the resulting dimer concentration trajectories and levels enable an evaluation of the monitoring and PAT approaches in a broad design space.

TABLE 2 Median at-line analysis delay and its median absolute deviation in parentheses

Experiment	Median analysis delay (min)
Run 1	5.6 (0.2)
Run 2	5.8 (0.4)
Run 3	13.9 (0.2)
Run 4	5.7 (0.2)
Run 5	5.5 (0.2)
Run 6	22.2 (5.3)

The median analysis delay is the median duration from sampling until SEC-HPLC injection and listed in Table 2. Samples from run 6 were analyzed with the largest median delay of 22.2 min. The higher permeate flux led to a shorter interval between samplings, which were conducted at each DV. Due to the fixed analysis duration of the SEC-HPLC method queueing of samples was required and resulted in a larger delay than for other runs. The continuation of the disassembly reaction until analysis theoretically results in an increase of measured dimer concentration compared with an analysis without any delay. This effect was considered negligible for this study as the analysis delay increased and the change in dimer concentration

decreased with increasing DV. The samples of all other runs were analyzed with median delays below 14 min. Nevertheless, this analysis delay can be reduced considerably applying on-line monitoring. This example emphasizes the value of the on-line monitoring approach proposed in this study. On-line monitoring is particularly of interest when processes with high permeate fluxes need to be characterized as the abovementioned time limitation causes larger deviations.

3.2 | In-line monitoring

The in-line monitoring results are depicted in Figure S2 and discussed in the Supporting Information Section S1. Briefly, the signals of all runs showed a similar progression and final values. As expected, a higher permeate flux resulted in a higher transmembrane pressure and higher NaCl or nucleic acid (impurity) levels resulted in a higher conductivity. In summary, the signals allow for a supervision of the diafiltration progress and performance. This monitoring approach enables an identification of deviations of the diafiltration buffer or feed. The buffer exchange is monitored directly by measuring actual retentate properties and is not estimated indirectly through DV which are usually based on influent (diafiltration buffer) and/or effluent (permeate) quantification.

3.3 | On-line monitoring

Figure 2 also shows the on-line monitoring results of the CFF processes. The on-line measured protein concentration and the at-line measured total Cp149 concentration were in good agreement and decreased over time. Both concentrations were determined using the respective 280 nm absorbance. Besides Cp149 dimers and VLPs, host cell nucleic acids and proteins contribute to the measured absorbance. The depletion of these impurities throughout the process leads to a decrease of the measured absorbance and thereby concentration. Using the absorbance for concentration determination of VLP-containing solutions furthermore leads to an overestimation due to the light scattering of VLPs. The decreasing VLP concentration (increasing dimer concentration) due to the disassembly leads to a reduced light scattering contribution to the absorbance over time. In this study, no scatter-correction was applied to the on-line or at-line absorbances but this is recommended if absolute concentration values are desired (e.g., see Porterfield & Zlotnick, 2010). For the at-line dimer concentration as the target variable, an overestimation due to light scattering was considered to be negligible because of the low molecular weight of the dimers. The stepwise decrease of the on-line measured protein concentration results from the abovementioned replacement of sample volume by diafiltration buffer. Other potential factors that could contribute to the decreasing total protein concentration are adsorption to the membrane, aggregation and removal by the measurement loop in-line filter, or undesired dilution due to higher diafiltration buffer inflow than permeate outflow. These factors were considered to play only a minor role under the investigated experimental conditions but the presented setup could enable the investigation of their influence in process optimization or characterization studies. It has to be noted that a change of the protein's UV absorption behavior due to the increasing urea concentration is expected but was not considered in this study.

As for the nature of the at-line Cp149 concentration and on-line protein concentration measurements, both are biased by UV-active impurities encapsulated in or bound to the VLPs. However, compared with the on-line measurement, the at-line SEC-HPLC measurement excludes impurities in solution which are smaller than dimers and are not bound to the dimers. The depletion of these small impurities throughout the diafiltration process explains the decreasing differences of on-line and at-line measured concentrations over time. The initially higher on-line measured protein concentration might also be enhanced by a lag of the diafiltration buffer inflow during the CFF startup leading to a concentration increase (feed sample was taken before the CFF start). Regarding the samples taken at 6 DV, the maximum observed deviation between the two measurements was 0.07 g L^{-1} in run 5. The on-line measured protein concentration is therefore an accurate representation of the total Cp149 concentration by at-line SEC-HPLC during the final phase of the investigated experiments.

The A260/A280 is an indicator for the nucleic acid content, in this case the impurity level, of a protein solution but is also expected to be influenced by light scattering of VLPs (Porterfield & Zlotnick, 2010) and the urea concentration (Hillebrandt et al., 2021). For run 5, the feed solution was spiked with less purified VLP solution and the highest initial A260/A280 of 0.74 was observed (Figure 2). For all experiments, the A260/A280 decreased to final values between 0.58 and 0.59, independently of the dimer concentration, initial impurity level, or NaCl concentration. Therefore, the A260/A280 could serve as a simple lumped quality indicator for the nucleic acid removal and disassembly progress or for the nucleic acid removal only if a scatter correction is applied. While the former approach only requires a bivariate UV signal, the latter requires at least three wavelengths (Porterfield & Zlotnick, 2010; Rolinger et al., 2020).

The SLS intensity of all experiments decreased with proceeding disassembly (Figure 2). When VLPs disassemble, this behavior is expected as the light scattering intensity decreases linearly with the particle concentration and with the sixth power of the particle diameter (Bohren & Huffman, 2004). For human papillomavirus VLPs, this behavior was previously observed in small-scale batch experiments (Mach et al., 2006). Cp149 VLPs are spherical particles with a diameter of approximately 30 nm and mainly consist of 240 dimers (Newman et al., 2003; Wynne et al., 1999). The absolute values of the SLS intensity show the same trend as the Cp149 total concentration reflecting the concentration-dependence.

The *z*-average describes the intensity-weighted harmonic mean of the particle size determined by DLS (Thomas, 1987). Compared with the SLS intensity, the recorded *z*-average is rather constant with more noise or oscillation (Figure 2). Runs 1, 2, 4, and 5 show a decrease of the *z*-average during the initial 50 min. As the *z*-average

determination by DLS relies on the Stokes–Einstein equation, it is sensitive to changes of the solvent viscosity (Thomas, 1987). The viscosity for the DLS measurements was set to the theoretical value of the urea-containing diafiltration buffer which had a higher viscosity than the feed buffer. Therefore, the initial *z*-average is overestimated and a decrease with increasing buffer exchange is expected. After 4 DV of diafiltration, corresponding to 33 min for run 6 and 57 min for runs 1–5, ideal buffer exchange leads to a composition with 98% diafiltration buffer (Kurnik et al., 1995). Therefore, only a minor viscosity change is expected toward the end of the process. Run 1 resulted in a final *z*-average of 24 nm, all other runs show final *z*-averages larger than 30 nm. In a previous work, HBcAg VLPs similar to Cp149 VLPs were disassembled using urea and resulted in subunits with 6 nm diameter (Lee & Tan, 2008). According to the abovementioned definitions of the *z*-average and light scattering intensity, even a small number of large particles in a polydisperse solution lead to a higher *z*-average than the size of the dominating species (Hassan et al., 2015; Stetefeld et al., 2016). In the case of VLP disassembly, the presence of aggregates or VLPs at the end of the disassembly leads to a higher *z*-average than the hydrodynamic diameter of the subunits, such as Cp149 dimers. The generally higher level of the *z*-average at higher protein concentrations might indicate a concentration-dependent aggregation tendency of Cp149 VLPs. Runs 1–5 show a *z*-average increase toward the end which could indicate aggregation. This increase was not observed for run 6, which was performed in less time. An increased aggregation tendency for longer processing time was similarly observed for the diafiltration-based reassembly using a similar monitoring setup (Rüdt et al., 2019). Another observation from that study was a *z*-average decrease for even longer processing times due to the retention of large aggregates by the measurement loop in-line filter. This behavior was also observed during the extended diafiltration of run 4 as shown in Figure S1. The underestimation of the *z*-average by DLS due to convective flow (Leung et al., 2006) was considered negligible for Cp149 VLPs and dimers due to the low flow rate. For a more detailed discussion, see Rüdt et al. (2019). In summary, the *z*-average showed to be not suitable for monitoring of the disassembly reaction but for monitoring of aggregation toward the end of the diafiltration-based disassembly process.

Second derivative UV spectroscopy was used to monitor changes in the microenvironment of tyrosine and tryptophan residues of Cp149 by determining the *a*/*b* ratio and the location of the minimum near 293 nm, respectively. An increasing *a*/*b* ratio indicates an increasing polarity of the microenvironment of tyrosine residues (Ragone et al., 1984) while a blue shift of the tryptophan band correlates to increasing polarity surrounding tryptophan residues (Mach & Middaugh, 1994). The microenvironment of amino acid residues buried within the protein (core) is regarded as non-polar compared with solvent-exposed residues. In previous works, second derivative UV spectroscopy was employed to monitor the disassembly of Norwalk VLPs (Ausar et al., 2006) and the reassembly of chimeric variants of Cp149 (Rüdt et al., 2019). In the latter, the increased surrounding polarity of certain tyrosine and tryptophan residues of HBcAg in the assembled state was attributed to their involvement in the VLP formation and the slope of the *a*/*b* ratio was identified as indicator for the assembly rate. Compared with those results, the disassembly experiments in this study showed inversed trends of the *a*/*b* ratio and the tryptophan band shift which is expected as the disassembly is the opposite reaction. The *a*/*b* ratio increased during all experiments and showed a similar curve shape over time as the dimer concentration (Figure 2) while the progression of the second derivative minimum around 293 nm (tryptophan band) was inversed. This indicates that the UV data contains information about the (dis-)assembly state of the VLPs. For runs 4 and 5, both values were approximately constant for the first 13 and 7 min, respectively. The initial conductivity in both runs, which is assumed to reflect the ionic strength to some extent, was higher due to the presence of NaCl in run 4 and nucleic acids in run 5. A higher ionic strength is known to stabilize the assembled state of Cp149 VLPs (Ceres & Zlotnick, 2002; Singh & Zlotnick, 2003). The higher VLP stability is supported by slower dimer concentration increase (slower disassembly) for run 4 compared with run 2 which was performed with the same initial protein concentration. Comparing run 5 with run 3 which were performed at a similar initial protein concentration but different impurity levels, both resulted in similar dimer concentration trajectories. The reason for that is most probably the low temporal resolution of the at-line analysis leading to the inability of detecting short-term changes. Interestingly, when comparing the initial and final dimer concentrations with the corresponding absolute *a*/*b* ratios, both quantities show a similar trend supporting their causal relationship. The similar *a*/*b* ratios of the runs 3 and 6 support the observation of similar dimer concentration profiles elaborated in Section 3.1. The capability to identify the dis- and reassembly state on-line with a high temporal resolution and without any prior calibration makes second derivative UV spectroscopy a valuable monitoring tool.

3.4 | Endpoint detection (process control)

The diafiltration-based VLP disassembly process requires a timely termination to avoid process-related product damage, for example due to extended exposure to shear forces or to elevated concentrations at the membrane surface. From an economic perspective, a timely termination is also desirable, for example to reduce buffer consumption or processing time. Especially since the disassembly reaction was observed to depend on liquid phase conditions rather than on time, a product-based monitoring is preferred over a simple time- or DV-based process termination decision. Two different methods were applied to detect the endpoint of the diafiltration-based disassembly process. The first was based on the results from second derivative UV spectroscopy (Section 3.3) which clearly indicated that the spectral data contain information on the disassembly reaction. Therefore, regression models were calibrated to directly correlate (latent) information in the on-line UV data to the dimer concentration. Once the models are calibrated, the dimer concentration can be traced without any additional at-line or off-line

analysis. One can then simply decide for a termination of the process based on the predicted concentration, for example when the slope falls below a predefined threshold. The second method was implemented to eliminate the need for previous at-line or off-line analyses. It simply uses univariate UV or SLS data to detect threshold values that correspond to the beginning of the plateau dimer concentration.

3.4.1 | Regression models

Regression models were calibrated by CV as described in Section 2.5. The runs for the calibration data set were selected manually as listed in Table 1. The selection was based on principal component analysis score plots aiming for a representative distribution of all occurring score values (data not shown).

Variable selection

Two PLS models (Models A and B) and one OLS model (Model C) were calibrated. Input data for the calibration were absorbances of either full recorded spectra (240–340 nm, Model A), a wavelength selection based on a genetic algorithm (Model B), or two individual wavelengths (Model C). After the optimal nLV was determined to be 3 using full spectra (cf. Model A), variable selection was carried out using the described genetic algorithm approach. It aimed to improve the model by selecting a set of wavelengths that achieves the best CV results. As the genetic algorithm is based on random number generation, the optimization was performed 10 times and the selections of each wavelength were accumulated. The number of genetic algorithm selections for each recorded wavelength are shown in Figure 3. For the sake of interpretation, the regression coefficients of Model A (nLV = 3) are also shown in Figure 3. Here, a high absolute value of a coefficient indicates a high relevance of the corresponding wavelength to the model. The extreme points (highest absolute values) of the regression coefficients are close to the most selected wavelengths by the genetic algorithm. This indicates that the PLS calibration algorithm optimized the model by considering similar wavelength regions important. However, the genetic algorithm approach allows to remove wavelengths that may contain irrelevant or unreliable information before the final PLS Model B is calibrated to achieve a better prediction (Andersen & Bro, 2010). The most selected regions (genetic algorithm) coincide to some extent with characteristic absorption peaks of the aromatic amino acids phenylalanine, tyrosine, and tryptophan (Hansen et al., 2013). This supports the found qualitative correlation of a/b ratio and second derivative minimum near 293 nm with the disassembly (Section 3.3). As neighboring variables in spectral data are usually highly correlated (Andersen & Bro, 2010), groups of wavelengths around the most selected regions (genetic algorithm) were manually selected to calibrate Model B and are highlighted in Figure 3. In contrast to the genetic algorithm results, omitting the wavelengths 240 and 241 nm improved the RMSECV and the RMSEP (data not shown). At these lower wavelengths in the mid-UV range, the peptide bond and cysteine residues contribute considerably to the absorption of proteins (Hansen et al., 2013). Therefore, the absorbance in this region might rather represent the overall protein concentration than the disassembly state.

Diode array detectors for acquisition of UV spectra are not commonly available or implemented in current manufacturing facilities of biopharmaceuticals. Inspired by the results of a recent study (Rolinger et al., 2021), the feasibility of a simple regression model based on only two individual wavelengths was evaluated. Therefore, an OLS regression model was calibrated using the calibration procedure as described in Section 2.5. The selection of the two wavelengths was achieved by calibrating a preliminary PLS model using full spectra and an nLV = 2. The resulting regression coefficients are shown in Figure 3. Interestingly, the regression coefficients are similar to ones using an nLV = 3 but shifted to higher wavelengths. The two wavelengths required to calibrate Model C were then chosen from the local extreme values of these regression coefficients of the preliminary nLV = 2 model. As mentioned above, wavelengths with higher absolute regression coefficients show a stronger contribution to the model, and neighboring UV wavelengths are usually highly correlated due to the nature of UV light absorption. Therefore, it was assumed that the data at wavelengths with extreme points in the regression coefficients are sufficient for an adequate prediction. Among the three extreme values, the best combination of two wavelengths was 284 and 309 nm (data not shown) and is marked in Figure 3.

Calibration and prediction

Figure 4 shows the predictions of the dimer concentration using the three regression models (A, B, and C). The results for each model are divided into the runs used for calibration and external runs as

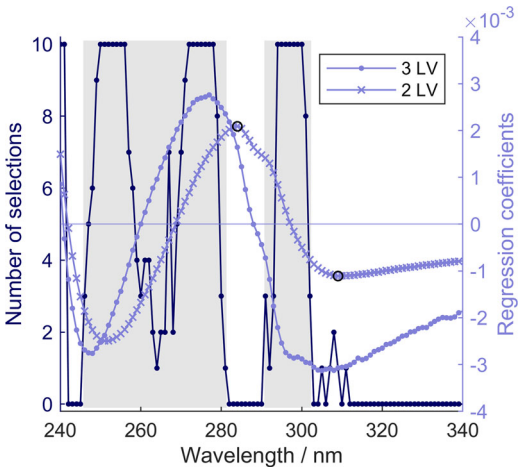

FIGURE 3 Variable selection by genetic algorithm and PLS regression coefficients. Both methods were performed with the full recorded wavelength range from 240 to 340 nm. Left axis (dark blue): Number of selections for an nLV = 3 PLS model by the genetic algorithm after 10 evaluations. Right axis (light blue): PLS regression coefficients for Model A (nLV = 3) and the preliminary model with an nLV = 2. The two wavelength ranges that were selected for Model B are highlighted in gray. The two wavelengths that were selected for Model C are indicated by black circles. Abbreviations: (n)LV, (number of) latent variables; PLS, partial least squares

independent validation set. Table 3 lists the characteristics of the model calibration and validation. In general, all models were calibrated successfully resulting in R^2 values above 0.980 and Q^2_{CV} values from 0.905 to 0.976. For the external validation set, Q^2_{Ext} values were in the range of the calibration values, indicating a strong predictive power of the models.

Regarding Model A, the progressions of the dimer concentration were well predicted by the model as shown in Figure 4. This also applies to the external validation set in which the maximum RMSEP occurred in run 3 with 0.064 g L^{-1} (Table S1). Most of the feed samples (0 min) were predicted less accurately than samples during the later stages. This can be expected as the feed samples vary most in their composition, for example in salt concentration or impurity profile. Throughout the diafiltration process, buffer exchange leads to a higher similarity of the samples, which are then mainly differing in dimer concentration. Additionally, the larger fraction of samples with rather constant conditions at the end of the process inherently leads to a stronger weighting of theses samples during calibration. Nevertheless, this behavior is desirable as an accurate prediction of these samples is required for a process termination decision.

Compared with Model A, the variable selection applied before the calibration of Model B improved the RMSECV by 0.051 g L^{-1}

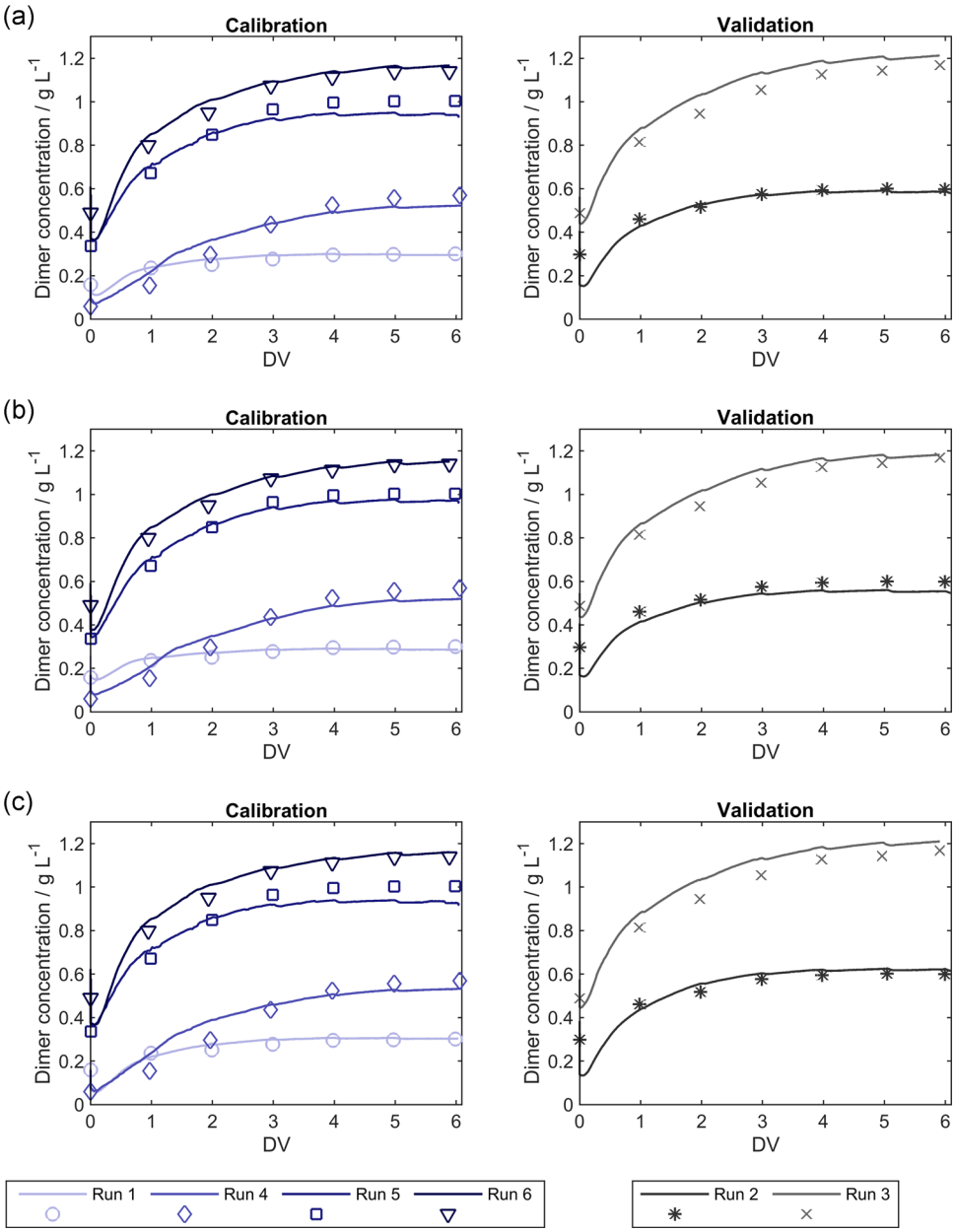

FIGURE 4 Calibration and external validation of regression models. Symbols represent reference measurements of the dimer concentration by at-line SEC-HPLC and continuous lines represent the model predictions based on the on-line UV absorbance measurements. (a)–(c) represent the predictions of the models A, B, and C, respectively. Abbreviations: DV, diafiltration volume; HPLC, high-performance liquid chromatography; SEC, size-exclusion chromatography; UV, ultraviolet light

TABLE 3 Results of the calibration by cross validation (CV) and external validation (Ext) of the three regression models A, B, and C

Model	Wavelengths (nm)	nLV (-)	R^2 (-)	RMSECV (g L^{-1})	Q^2_{CV} (-)	Q^2_{Ext} (-)
A	240–340	3	0.985	0.106	0.909	0.955
B	246–281, 291–302	3	0.990	0.055	0.976	0.963
C	284, 309	2	0.981	0.067	0.964	0.948

Note: The models were calibrated with absorbance data of different wavelengths regions as listed.
Abbreviations: nLV, number of latent variables; RMSECV, root mean square error of cross validation.

(48%). This was, along with R^2, Q^2_{CV}, and Q^2_{Ext}, the best of the three models. In comparison with Model B, other recent UV-based PLS models (Rolinger et al., 2021; Rüdt et al., 2019; Zobel-Roos et al., 2017) achieved comparable R^2 and Q^2_{CV} with 0.995–0.999 and 0.984–0.999, respectively. In accordance with the lower RMSECV, the calibration set was predicted more accurately. This improvement was most pronounced toward the end of run 5, which had a higher impurity level of the feed solution. A potential explanation is that some impurities were not depleted throughout the diafiltration and led to a less accurate prediction by Model A. The variable selection applied for Model B then leads to a focus on spectral regions that allow for a prediction less biased by the impurities. The predictions of the external validation set were on average improved whereas the RMSEP decreased by 0.016 g L^{-1} for run 3 and increased by 0.005 g L^{-1} for run 2 (Table S1).

Model C was calibrated and applied using only two wavelengths. Regardless of the strong reduction of input data, the predictions were comparable with or only slightly less accurate than Model A. These remarkable results are assumed to arise from the combination of the selected wavelengths. The first, 284 nm, is close to 280 nm, which is considered as the peak of the lumped absorption of aromatic amino acids and therefore commonly used for protein concentration determination. At the second wavelength of 309 nm, the UV absorption of proteins is considerably lower and light scattering contributes increasingly to the overall absorbance. This is supported by similar curve shapes of the on-line 309 nm absorbance (cf. Section 3.4.2) and the SLS intensity. The latter coincides with the disassembly progress as shown in Section 3.3. Therefore, it is assumed that Model C combines the information on concentration and degree of disassembly from the input data to predict the dimer concentration.

Overall, the results indicate that regression models are capable of predicting the dimer concentration at varying protein concentrations and liquid phase conditions, namely salt concentration and impurity level. The accurate prediction of the dimer concentration progress, especially toward the end of the process, enables an accurate endpoint detection. As quenching the VLP disassembly reaction is not easily possible, on-line UV monitoring in conjunction with PLS models is furthermore a valuable tool to characterize diafiltration-based disassembly in process development.

Application for detection

Data of Model B were used to demonstrate a potential endpoint detection approach as a stagnating dimer concentration indicates the endpoint of the disassembly reaction. Therefore, first derivatives of the predicted dimer concentrations were approximated by calculating the difference using a backward-oriented moving window of ~1 min corresponding to 50 data points. A larger window usually leads to lower noise but also to a larger detection delay. The results are shown in Figure 5 together with the at-line measured dimer concentration for comparison. The ideal process endpoint was defined as the beginning of the at-line dimer concentration plateau which was defined by a slope ≤0.0013 g L^{-1} min^{-1}. This slope was also used as a threshold for the endpoint detection based on the predicted dimer concentration. To avoid unintended triggering during the startup phase, the detection was activated only after 10 min. For a technical process implementation, this activation is suggested to be based on the conductivity and/or pH signal. The detected endpoints are also shown in Figure 5. In all runs, the derivative increased to a global maximum and then decreased non-monotonically. Besides high frequency noise, the derivative showed distinct valleys which resulted from the abovementioned concentration decrease caused by sampling for at-line analysis. These small but rapid concentration changes lead to more pronounced disturbances in the first derivative signals. To enable an automated endpoint detection without additional data processing, the endpoint detection was disabled for 4 min after each sampling to avoid unintended triggering. In an industrial setting, the sample volume would be much smaller in relation to the retentate volume and the disturbance of the UV signal by sampling is expected to be negligible.

Except for run 6, deviations of the detected endpoint from the beginning of the dimer concentration plateau were 12 min at most with a root mean square error (RMSE) of 9 min and within ±1 DV. No endpoint was detected in run 6 as the lowest derivative was just above (0.5×10^{-3} g L^{-1} min^{-1}) the threshold value. The threshold would be reached using a lower window for the approximate derivative which led, however, to unsatisfying noise reduction for other runs (data not shown). Based on this single example, using universal data processing parameters is not suggested for varying permeate fluxes. It has to be noted that the plateau onset itself was identified based on the discrete samples with an interval of ~14 min (~7 min for run 6) and should be regarded as an approximation. The discretization by sampling (at each DV) mathematically leads to an underestimation of the dimer concentration slope while the use of a threshold value potentially detects the plateau onset too late. This also demonstrates the advantage of an automated endpoint detection based on continuously acquired on-line data: decisions can be made faster and are not limited to the sampling interval. The limited accuracy of the plateau onset has to be considered when evaluating the reliability of

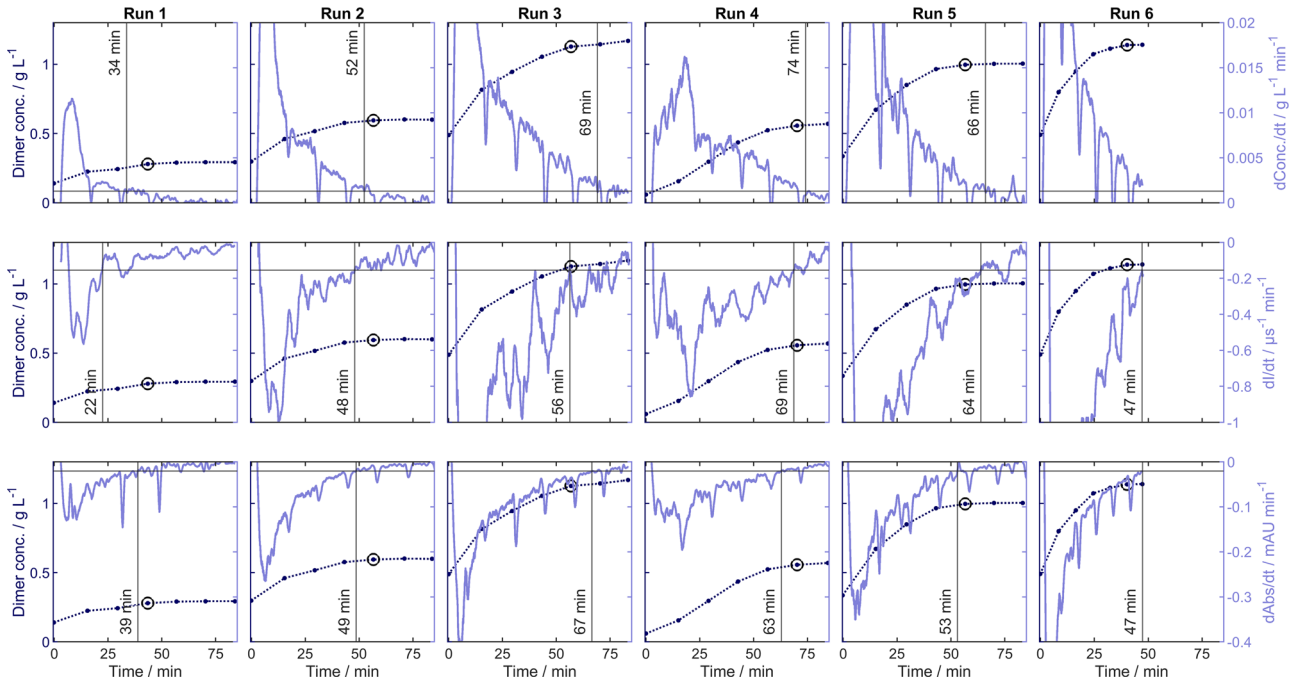

FIGURE 5 Endpoint detection. Left axis (dark blue): dimer concentration by at-line SEC-HPLC with dotted lines to guide the eye and the beginning of the concentration plateau indicated by a black circle. Right axis (light blue): approximate first derivative of the predicted dimer concentration by Model B (top), the SLS intensity (middle), and the absorbance at 309 nm (bottom) calculated by a moving difference with a window of ~1, ~3, and ~1 min, respectively. Horizontal lines indicate the threshold value for endpoint detection. For exceptions to triggering at the threshold value, see Section 3.4. Vertical lines indicate the detected endpoint according to the sensor signals predicted dimer concentration, SLS intensity, and 309 nm absorbance. Abbreviations: Abs, absorbance; conc., concentration; HPLC, high-performance liquid chromatography; I, SLS intensity; SEC, size-exclusion chromatography; SLS, static light scattering; *t*, time

the endpoint detection approaches, so that an endpoint detection within ±1 DV of the plateau onset was considered as reliable in this study. In this regard, the process endpoint was successfully detected for runs 1–5 while the signal was only close to the threshold value in run 6. However, the run-to-run variability in a fully developed and established process should be much lower than the conditions screened in this study. Together with a fine tuning of the detection parameters, an even improved performance of the detection approaches can be expected.

3.4.2 | Univariate approaches

Besides the regression models, two calibration-free approaches were theoretically investigated for their ability to detect the process endpoint. The first approach was chosen based on the observed visual correlation between the SLS intensity and the dimer concentration. The second approach was chosen based on the expected light scattering contribution to the 309 nm absorbance and its good performance as input parameter for Model C. As the SLS intensity decreases due to the disassembly of VLP, a derivative approximating zero indicates the end of the disassembly reaction. Therefore, first derivatives of SLS intensity and 309 nm absorbance were approximated as described in Section "Application for detection" using a moving difference with a window of 19 data points (~3 min) and 50 data points (~1 min), respectively. The results are also shown in Figure 5. For both approaches and all runs, the derivative decreased to a global minimum and then increased non-monotonically. Compared with the SLS measurements at 633 nm, the 309 nm absorbance is more sensitive to changes in the protein concentration due to absorption and a higher SLS intensity according to the Rayleigh approximation. Consequently, the distinct disturbances (valleys) after sampling were more pronounced for the 309 nm absorbance. As the direction of these disturbances did not interfere with the automated endpoint detection, a deactivation after sampling is not required in this case.

For each of the two derivatives, a common threshold value for all runs was required to trigger the endpoint detection. Thus, a grid search was performed to minimize the distances between the detected times and the corresponding beginning of the dimer concentration plateau. Briefly, 1000 evenly spaced threshold values were generated between the lowest derivative value at a plateau onset and the highest derivative value of run 6. The latter was required to enable a detection in all runs as the maximum derivative values of run 6 were lower than for the other runs. The threshold values which achieved the lowest RMSE between the detected times and the plateau onset were −0.1544 µs^{-1} min^{-1} with an RMSE of 10 min for SLS intensity and −0.02 mAU min^{-1} with an RMSE of 7 min for 309 nm absorbance. Both RMSEs were comparable with the detection based on the predicted dimer concentrations (RMSE of 9 min)

and resulted in predominantly similar detections (Figure 5). Except for run 1, the detected SLS-based endpoints deviate maximum 9 min and ±1 DV from the beginning of the plateau. For run 1, the early detection resulted from a local maximum of the derivative. Due to the generally lower concentration in run 1, concentration changes due to sampling have a greater impact on the SLS intensity potentially leading to the local maximum. Using the 309 nm absorbance resulted in an improved endpoint detection for run 1 and similar or slightly less accurate detections for the other runs. All deviations were below 10 min and within ±1 DV of the plateau onset. The assumed combination of UV absorption and scattering seems less sensitive to disturbances which is also reflected in less noise apart from the sampling-related disturbances. This is particularly beneficial as it enables rapid and simple process control with a standard UV sensor. The latest/least detection for run 6 is in accordance with the results based on the predicted dimer concentrations (Section "Application for detection"). This raises the question if this trend originates from an underlying minor time dependence of the disassembly reaction which cannot be resolved by at-line analysis or from a non-optimized data processing and detection algorithm for higher permeate fluxes. As stated in Section 3.1, this would be interesting to investigate in further studies. Similarly to the regression model, the univariate approaches reliably detected the end of the disassembly for a range of product concentrations and liquid phase conditions demonstrating its applicability. When changing the permeate flux, an additional detection parameter adjustment might be beneficial.

3.4.3 | Industrial considerations and potential

From an industrial perspective, the implementation would include model/control robustness testing with regard to run-to-run variability and hardware implementation at a larger scale. Robustness testing for the range of manufacturing specifications in terms of protein concentration, buffer pH and concentration, and other process parameters would be performed to assess the performance of the implemented model/control at the edge of the design space. The present study already demonstrates the capabilities of the developed framework under a range of conditions and provides the groundwork for this robustness testing. As shown above, a considerable monitoring and control is enabled by the UV absorbance measurement at one or two wavelengths; thus a standard UV sensor would be sufficient hardware for implementation. Currently commercially available pilot and process scale CFF units usually contain a UV sensor in the permeate line (e.g., ÄKTA UniFlux/readyflux (XL) by Cytiva, Cogent by Merck Millipore, KrosFlo KMPi/KTF by Repligen, and Sartoflow 1000/4500 by Sartorius Stedim Biotech). In-line variable pathlength UV absorbance measurements have been shown to perform well in the CFF retentate (Rolinger et al., 2020) for processes with high protein concentrations. Since VLPs are usually processed at much lower concentrations, in-line UV monitoring in the retentate should be possible with standard equipment and a low degree of customization. In-line measurements further provide continuous data over process time without any additional delays often caused by off-line measurements.

The developed framework aligns well with the demands for the Quality by Design approach suggested regulatory authorities, which aims for a knowledge-based development of processes, cf. Q11 and Q8(R2) guidelines (ICH Expert Working Group, 2009, 2012). The implementation of multiple sensors enables tracing of disassembly trajectories under varying liquid phase and processing conditions. Furthermore, meaningful and reliable sensors to control critical quality attributes can be identified during the development phase. This knowledge can aid in decision-making during manufacturing process development and operation. Overall, the presented approach would enable a larger design space of processes and thereby enhanced manufacturing flexibility (ICH Expert Working Group, 2012).

4 | CONCLUSIONS

In this study, a process monitoring framework consisting of in-line, on-line, and at-line analysis was implemented to investigate the diafiltration-based disassembly of HBcAg VLPs. The framework provides data on multiple characteristics simultaneously such as filtration performance, liquid phase conditions (diafiltration progress), and product properties. For the latter, regression models in combination with on-line UV spectra accurately predicted the dimer (VLP subunit) concentration in the CFF unit. Univariate UV and SLS signals were also identified as qualitative indicators of disassembly progress. Here, the 309 nm absorbance and simple mathematical operations were utilized to successfully detect the endpoint of the diafiltration-based disassembly. It was concluded that the 309 nm absorbance combines UV absorption and light scattering and therefore indicates a combination of protein properties such as concentration and particle size. Another interesting process-related observation was that a reduction in processing time did not result in a slower disassembly, although this should be confirmed by further research.

The presented framework closes the gap in process monitoring between capture/purification and reassembly for VLP processes that are based on dis- and reassembly. It therefore forms the basis for an end-to-end PAT approach for VLP downstream processing. In future, the developed monitoring framework could be applied to other non-enveloped VLPs, for example derived from papillomaviruses or Norwalk viruses. Changes in SLS intensity and UV spectra due to disassembly are also known for these VLPs, which makes a successful transfer likely. The presented combination of diafiltration and on-line monitoring of product properties might also be beneficial for other biochemical reactions such as inclusion body solubilization and refolding. Overall, the varying complexity of the developed PAT approaches enables potential applications in various fields, ranging from reaction analysis over process development to manufacturing. Regarding current regulatory initiatives such as Quality by Design, this broad complexity scale is particularly beneficial. Complex experimental setups, equipment, and models facilitate a thorough process characterization and the identification of viable signals for process

control. This prior knowledge enables the implementation of simple and efficient monitoring and control at manufacturing scale.

ACKNOWLEDGMENTS

This project received funding from Deutsche Forschungsgemeinschaft (DFG) in the frame of SPP 1934, project number 273937032. The authors express their gratitude to Adam Zlotnick and Kim Young for the provision with VLP production plasmids. The authors would like to thank Robin Schiemer for thoroughly reviewing the manuscript and providing valuable suggestions.

CONFLICTS OF INTEREST

The authors declare no conflicts of interests.

AUTHOR CONTRIBUTIONS

Jürgen Hubbuch initiated the work. Nils Hillebrandt evolved the concepts and setup presented in this manuscript, performed and supervised experimental work, analyzed and interpreted the data, and drafted the final manuscript. Philipp Vormittag aided in conceptualization and supervision of the experimental work. Annabelle Dietrich performed experimental work. Nils Hillebrandt, Philipp Vormittag, Annabelle Dietrich, and Jürgen Hubbuch reviewed and approved the final manuscript.

DATA AVAILABILITY STATEMENT

The data that support the findings of this study are available from the corresponding author upon reasonable request.

ORCID

Nils Hillebrandt http://orcid.org/0000-0002-3097-3140

REFERENCES

Andersen, C. M., & Bro, R. (2010). Variable selection in regression—A tutorial. *Journal of Chemometrics*, *24*(11–12), 728–737. https://doi.org/10.1002/cem.1360

Ashley, C. E., Carnes, E. C., Phillips, G. K., Durfee, P. N., Buley, M. D., Lino, C. A., Padilla, D. P., Phillips, B., Carter, M. B., Willman, C. L., Brinker, C. J., Caldeira Jdo, C., Chackerian, B., Wharton, W., & Peabody, D. S. (2011). Cell-specific delivery of diverse cargos by bacteriophage MS2 virus-like particles. *ACS Nano*, *5*(7), 5729–5745. https://doi.org/10.1021/nn201397z

Ausar, S. F., Foubert, T. R., Hudson, M. H., Vedvick, T. S., & Middaugh, C. R. (2006). Conformational stability and disassembly of Norwalk virus-like particles. *Journal of Biological Chemistry*, *281*(28), 19478–19488. https://doi.org/10.1074/jbc.M603313200

Bohren, C. F., & Huffman, D. R. (2004). *Absorption and scattering of light by small particles*. Wiley-VCH Verlag GmbH & Co. KGaA. https://doi.org/10.1002/9783527618156

Carreira, A., Menéndez, M., Reguera, J., Almendral, J. M., & Mateu, M. G. (2004). In vitro disassembly of a parvovirus capsid and effect on capsid stability of heterologous peptide insertions in surface loops. *Journal of Biological Chemistry*, *279*(8), 6517–6525. https://doi.org/10.1074/jbc.M307662200

Carvalho, S. B., Silva, R. J. S., Moleirinho, M. G., Cunha, B., Moreira, A. S., Xenopoulos, A., Alves, P. M., Carrondo, M. J. T., & Peixoto, C. (2019). Membrane-based approach for the downstream processing of influenza virus-like particles. *Biotechnology Journal*, *14*(8), 1800570. https://doi.org/10.1002/biot.201800570

Ceres, P., & Zlotnick, A. (2002). Weak protein–protein interactions are sufficient to drive assembly of hepatitis B virus capsids. *Biochemistry*, *41*(39), 11525–11531. https://doi.org/10.1021/bi0261645

Cerqueira, C., Thompson, C. D., Day, P. M., Pang, Y.-Y. S., Lowy, D. R., & Schiller, J. T. (2017). Efficient production of papillomavirus gene delivery vectors in defined in vitro reactions. *Molecular Therapy—Methods & Clinical Development*, *5*, 165–179. https://doi.org/10.1016/j.omtm.2017.04.005

Chandramohan, D., Zongo, I., Sagara, I., Cairns, M., Yerbanga, R.-S., Diarra, M., Nikièma, F., Tapily, A., Sompougdou, F., Issiaka, D., Zoungrana, C., Sanogo, K., Haro, A., Kaya, M., Sienou, A. A., Traore, S., Mahamar, A., Thera, I., Diarra, K., … Greenwood, B. (2021). Seasonal malaria vaccination with or without seasonal malaria chemoprevention. *New England Journal of Medicine*, *385*(11), 1005–1017. https://doi.org/10.1056/NEJMoa2026330

Chu, K.-B., Kang, H.-J., Yoon, K.-W., Lee, H.-A., Moon, E.-K., Han, B.-K., & Quan, F.-S. (2021). Influenza virus-like particle (VLP) vaccines expressing the SARS-CoV-2 S glycoprotein, S1, or S2 domains. *Vaccines*, *9*(8), 920. https://doi.org/10.3390/vaccines9080920

Deep, K., Singh, K. P., Kansal, M. L., & Mohan, C. (2009). A real coded genetic algorithm for solving integer and mixed integer optimization problems. *Applied Mathematics and Computation*, *212*(2), 505–518. https://doi.org/10.1016/j.amc.2009.02.044

de Jong, S. (1993). SIMPLS: An alternative approach to partial least squares regression. *Chemometrics and Intelligent Laboratory Systems*, *18*(3), 251–263. https://doi.org/10.1016/0169-7439(93)85002-X

Gasteiger, E., Hoogland, C., Gattiker, A., Duvaud, S., Wilkins, M. R., Appel, R. D., & Bairoch, A. (2005). Protein identification and analysis tools on the ExPASy server. In J. M. Walker (Ed.), *The proteomics protocols handbook* (pp. 571–607). Humana Press. https://doi.org/10.1385/1-59259-890-0:571

Großhans, S., Rüdt, M., Sanden, A., Brestrich, N., Morgenstern, J., Heissler, S., & Hubbuch, J. (2018). In-line Fourier-transform infrared spectroscopy as a versatile process analytical technology for preparative protein chromatography. *Journal of Chromatography A*, *1547*, 37–44. https://doi.org/10.1016/j.chroma.2018.03.005

Grzenia, D. L., Carlson, J. O., & Wickramasinghe, S. R. (2008). Tangential flow filtration for virus purification. *Journal of Membrane Science*, *321*(2), 373–380. https://doi.org/10.1016/j.memsci.2008.05.020

Hansen, S. K., Jamali, B., & Hubbuch, J. (2013). Selective high throughput protein quantification based on UV absorption spectra. *Biotechnology and Bioengineering*, *110*(2), 448–460. https://doi.org/10.1002/bit.24712

Hartzell, E. J., Lieser, R. M., Sullivan, M. O., & Chen, W. (2020). Modular hepatitis B virus-like particle platform for biosensing and drug delivery. *ACS Nano*, *14*(10), 12642–12651. https://doi.org/10.1021/acsnano.9b08756

Hassan, P. A., Rana, S., & Verma, G. (2015). Making sense of Brownian motion: Colloid characterization by dynamic light scattering. *Langmuir: The ACS Journal of Surfaces and Colloids*, *31*(1), 3–12. https://doi.org/10.1021/la501789z

Hillebrandt, N., Vormittag, P., Bluthardt, N., Dietrich, A., & Hubbuch, J. (2020). Integrated process for capture and purification of virus-like particles: Enhancing process performance by cross-flow filtration. *Frontiers in Bioengineering and Biotechnology*, *8*, 489. https://doi.org/10.3389/fbioe.2020.00489

Hillebrandt, N., Vormittag, P., Dietrich, A., Wegner, C. H., & Hubbuch, J. (2021). Process development for cross-flow diafiltration-based VLP disassembly: A novel high-throughput screening approach. *Biotechnology and Bioengineering*, *118*(10), 3926–3940. https://doi.org/10.1002/bit.27868

Holmes, K., Shepherd, D. A., Ashcroft, A. E., Whelan, M., Rowlands, D. J., & Stonehouse, N. J. (2015). Assembly pathway of hepatitis B core

virus-like particles from genetically fused dimers. *Journal of Biological Chemistry*, *290*(26), 16238–16245. https://doi.org/10.1074/jbc.M114.622035

ICH Expert Working Group. (2009). *Q8(R2) guideline—Pharmaceutical development*. International Conference on Harmonisation of Technical Requirements for Registration of Pharmaceuticals for Human Use. https://database.ich.org/sites/default/files/Q8%28R2%29Guideline.pdf

ICH Expert Working Group. (2012). *Q11 guideline—Development and manufacture of drug substances*. International Conference on Harmonisation of Technical Requirements for Registration of Pharmaceuticals for Human Use. https://database.ich.org/sites/default/files/Q11Guideline.pdf

Kalbfuss, B., Genzel, Y., Wolff, M., Zimmermann, A., Morenweiser, R., & Reichl, U. (2007). Harvesting and concentration of human influenza A virus produced in serum-free mammalian cell culture for the production of vaccines. *Biotechnology and Bioengineering*, *97*(1), 73–85. https://doi.org/10.1002/bit.21139

Karpenko, L. I., Ivanisenko, V. A., Pika, I. A., Chikaev, N. A., Eroshkin, A. M., Veremeiko, T. A., & Ilyichev, A. A. (2000). Insertion of foreign epitopes in HBcAg: How to make the chimeric particle assemble. *Amino Acids*, *18*(4), 329–337. https://doi.org/10.1007/s007260070072

Kaufmann, A. M., Nieland, J. D., Jochmus, I., Baur, S., Friese, K., Gabelsberger, J., Gieseking, F., Gissmann, L., Glasschröder, B., Grubert, T., Hillemanns, P., Höpfl, R., Ikenberg, H., Schwarz, J., Karrasch, M., Knoll, A., Küppers, V., Lechmann, M., Lelle, R. J., … Schneider, A. (2007). Vaccination trial with HPV16 L1E7 chimeric virus-like particles in women suffering from high grade cervical intraepithelial neoplasia (CIN 2/3). *International Journal of Cancer*, *121*(12), 2794–2800. https://doi.org/10.1002/ijc.23022

Kessler, W. (2006). *Multivariate datenanalyse*. Wiley. https://doi.org/10.1002/9783527610037

Kingston, N. J., Kurtovic, L., Walsh, R., Joe, C., Lovrecz, G., Locarnini, S., Beeson, J. G., & Netter, H. J. (2019). Hepatitis B virus-like particles expressing Plasmodium falciparum epitopes induce complement-fixing antibodies against the circumsporozoite protein. *Vaccine*, *37*(12), 1674–1684. https://doi.org/10.1016/j.vaccine.2019.01.056

Klamp, T., Schumacher, J., Huber, G., Kühne, C., Meissner, U., Selmi, A., Hiller, T., Kreiter, S., Markl, J., Türeci, Ö., & Sahin, U. (2011). Highly specific auto-antibodies against claudin-18 isoform 2 induced by a chimeric HBcAg virus-like particle vaccine kill tumor cells and inhibit the growth of lung metastases. *Cancer Research*, *71*(2), 516–527. https://doi.org/10.1158/0008-5472.CAN-10-2292

Kurnik, R. T., Yu, A. W., Blank, G. S., Burton, A. R., Smith, D., Athalye, A. M., & van Reis, R. (1995). Buffer exchange using size exclusion chromatography, countercurrent dialysis, and tangential flow filtration: Models, development, and industrial application. *Biotechnology and Bioengineering*, *45*(2), 149–157. https://doi.org/10.1002/bit.260450209

Lee, K. W., & Tan, W. S. (2008). Recombinant hepatitis B virus core particles: Association, dissociation and encapsidation of green fluorescent protein. *Journal of Virological Methods*, *151*(2), 172–180. https://doi.org/10.1016/j.jviromet.2008.05.025

Leung, A. B., Suh, K. I., & Ansari, R. R. (2006). Particle-size and velocity measurements in flowing conditions using dynamic light scattering. *Applied Optics*, *45*(10), 2186–2190. https://doi.org/10.1364/AO.45.002186

Liew, M. W. O., Chuan, Y. P., & Middelberg, A. P. J. (2012). Reactive diafiltration for assembly and formulation of virus-like particles. *Biochemical Engineering Journal*, *68*, 120–128. https://doi.org/10.1016/j.bej.2012.07.009

Lin, S.-Y., Chiu, H.-Y., Chiang, B.-L., & Hu, Y.-C. (2015). Development of EV71 virus-like particle purification processes. *Vaccine*, *33*(44), 5966–5973. https://doi.org/10.1016/j.vaccine.2015.04.077

Mach, H., & Middaugh, C. R. (1994). Simultaneous monitoring of the environment of tryptophan, tyrosine, and phenylalanine residues in proteins by near-ultraviolet second-derivative spectroscopy. *Analytical Biochemistry*, *222*(2), 323–331. https://doi.org/10.1006/abio.1994.1499

Mach, H., Volkin, D. B., Troutman, R. D., Wang, B., Luo, Z., Jansen, K. U., & Shi, L. (2006). Disassembly and reassembly of yeast-derived recombinant human papillomavirus virus-like particles (HPV VLPs). *Journal of Pharmaceutical Sciences*, *95*(10), 2195–2206. https://doi.org/10.1002/jps.20696

McCarthy, M. P., White, W. I., Palmer-Hill, F., Koenig, S., & Suzich, J. A. (1998). Quantitative disassembly and reassembly of human papillomavirus type 11 viruslike particles in vitro. *Journal of Virology*, *72*(1), 32–41. https://doi.org/10.1128/JVI.72.1.32-41.1998

Mellado, M. C. M., Mena, J. A., Lopes, A., Ramírez, O. T., Carrondo, M. J. T., Palomares, L. A., & Alves, P. M. (2009). Impact of physicochemical parameters on in vitro assembly and disassembly kinetics of recombinant triple-layered rotavirus-like particles. *Biotechnology and Bioengineering*, *104*(4), https://doi.org/10.1002/bit.22430

Mohsen, M., Gomes, A., Vogel, M., & Bachmann, M. (2018). Interaction of viral capsid-derived virus-like particles (VLPs) with the innate immune system. *Vaccines*, *6*(3), 37. https://doi.org/10.3390/vaccines6030037

Moleirinho, M. G., Rosa, S., Carrondo, M., Silva, R., Hagner-McWhirter, Å., Ahlén, G., Lundgren, M., Alves, P. M., & Peixoto, C. (2018). Clinical-grade oncolytic adenovirus purification using polysorbate 20 as an alternative for cell lysis. *Current Gene Therapy*, *18*(6), 366–374. https://doi.org/10.2174/1566523218666181109141257

Negrete, A., Pai, A., & Shiloach, J. (2014). Use of hollow fiber tangential flow filtration for the recovery and concentration of HIV virus-like particles produced in insect cells. *Journal of Virological Methods*, *195*, 240–246. https://doi.org/10.1016/j.jviromet.2013.10.017

Neirynck, S., Deroo, T., Saelens, X., Vanlandschoot, P., Jou, W. M., & Fiers, W. (1999). A universal influenza A vaccine based on the extracellular domain of the M2 protein. *Nature Medicine*, *5*(10), 1157–1163. https://doi.org/10.1038/13484

Newman, M., Suk, F.-M., Cajimat, M., Chua, P. K., & Shih, C. (2003). Stability and morphology comparisons of self-assembled virus-like particles from wild-type and mutant human hepatitis B virus capsid proteins. *Journal of Virology*, *77*(24), 12950–12960. https://doi.org/10.1128/JVI.77.24.12950-12960.2003

Nilsson, J., de Jong, S., & Smilde, A. K. (1997). Multiway calibration in 3D QSAR. *Journal of Chemometrics*, *11*(6), 511–524. https://doi.org/10.1002/(SICI)1099-128X(199711/12)11:6%3C511::AID-CEM488%3E3.0.CO;2-W

Palladini, A., Thrane, S., Janitzek, C. M., Pihl, J., Clemmensen, S. B., de Jongh, W. A., Clausen, T. M., Nicoletti, G., Landuzzi, L., Penichet, M. L., Balboni, T., Ianzano, M. L., Giusti, V., Theander, T. G., Nielsen, M. A., Salanti, A., Lollini, P. L., Nanni, P., & Sander, A. F. (2018). Virus-like particle display of HER2 induces potent anti-cancer responses. *Oncoimmunology*, *7*(3), e1408749. https://doi.org/10.1080/2162402X.2017.1408749

Peixoto, C., Sousa, M. F. Q., Silva, A. C., Carrondo, M. J. T., & Alves, P. M. (2007). Downstream processing of triple layered rotavirus like particles. *Journal of Biotechnology*, *127*(3), 452–461. https://doi.org/10.1016/j.jbiotec.2006.08.002

Petrovskis, I., Lieknina, I., Dislers, A., Jansons, J., Bogans, J., Akopjana, I., Zakova, J., & Sominskaya, I. (2021). Production of the HBc protein from different HBV genotypes in E. coli. Use of reassociated HBc VLPs for packaging of ss- and dsRNA. *Microorganisms*, *9*(2), 283. https://doi.org/10.3390/microorganisms9020283

Phillips, A. T., & Signs, M. W. (2004). Desalting, concentration, and buffer exchange by dialysis and ultrafiltration. *Current Protocols in Protein*

Science, *38*(1), 1–15. https://doi.org/10.1002/0471140864.ps0404s38

Porterfield, J. Z., & Zlotnick, A. (2010). A simple and general method for determining the protein and nucleic acid content of viruses by UV absorbance. *Virology*, *407*(2), 281–288. https://doi.org/10.1016/j.virol.2010.08.015

Porterfield, J. Z., Dhason, M. S., Loeb, D. D., Nassal, M., Stray, S. J., & Zlotnick, A. (2010). Full-length hepatitis B virus core protein packages viral and heterologous RNA with similarly high levels of cooperativity. *Journal of Virology*, *84*(14), 7174–7184. https://doi.org/10.1128/JVI.00586-10

Ragone, R., Colonna, G., Balestrieri, C., Servillo, L., & Irace, G. (1984). Determination of tyrosine exposure in proteins by second-derivative spectroscopy. *Biochemistry*, *23*(8), 1871–1875. https://doi.org/10.1021/bi00303a044

Roldão, A., Mellado, M. C. M., Lima, J. C., Carrondo, M. J. T., Alves, P. M., & Oliveira, R. (2012). On the effect of thermodynamic equilibrium on the assembly efficiency of complex multi-layered virus-like particles (VLP): The case of rotavirus VLP. *PLoS Computational Biology*, *8*(2), e1002367. https://doi.org/10.1371/journal.pcbi.1002367

Rolinger, L., Rüdt, M., Diehm, J., Chow-Hubbertz, J., Heitmann, M., Schleper, S., & Hubbuch, J. (2020). Multi-attribute PAT for UF/DF of proteins—Monitoring concentration, particle sizes, and buffer exchange. *Analytical and Bioanalytical Chemistry*, *412*(9), 2123–2136. https://doi.org/10.1007/s00216-019-02318-8

Rolinger, L., Rüdt, M., & Hubbuch, J. (2021). A multisensor approach for improved protein A load phase monitoring by conductivity-based background subtraction of UV spectra. *Biotechnology and Bioengineering*, *118*(2), 905–917. https://doi.org/10.1002/bit.27616

Rüdt, M., Vormittag, P., Hillebrandt, N., & Hubbuch, J. (2019). Process monitoring of virus-like particle reassembly by diafiltration with UV/Vis spectroscopy and light scattering. *Biotechnology and Bioengineering*, *116*(6), 1366–1379. https://doi.org/10.1002/bit.26935

Rutgers, T., Gordon, D., Gathoye, A. M., Hollingdale, M., Hockmeyer, W., Rosenberg, M., & Wilde, M. de (1988). Hepatitis B surface antigen as carrier matrix for the repetitive epitope of the circumsporozoite protein of Plasmodium Falciparum. *Nature Biotechnology*, *6*(9), 1065–1070. https://doi.org/10.1038/nbt0988-1065

Schumacher, J., Bacic, T., Staritzbichler, R., Daneschdar, M., Klamp, T., Arnold, P., Jägle, S., Türeci, Ö., Markl, J., & Sahin, U. (2018). Enhanced stability of a chimeric hepatitis B core antigen virus-like-particle (HBcAg-VLP) by a C-terminal linker-hexahistidine-peptide. *Journal of Nanobiotechnology*, *16*(1), 39. https://doi.org/10.1186/s12951-018-0363-0

Sedlik, C., Saron, M. F., Sarraseca, J., Casal, I., & Leclerc, C. (1997). Recombinant parvovirus-like particles as an antigen carrier: A novel nonreplicative exogenous antigen to elicit protective antiviral cytotoxic T cells. *Proceedings of the National Academy of Sciences of the United States of America*, *94*(14), 7503–7508. https://doi.org/10.1073/pnas.94.14.7503

Shan, W., Zhang, D., Wu, Y., Lv, X., Hu, B., Zhou, X., Ye, S., Bi, S., Ren, L., & Zhang, X. (2018). Modularized peptides modified HBc virus-like particles for encapsulation and tumor-targeted delivery of doxorubicin. *Nanomedicine: Nanotechnology, Biology and Medicine*, *14*(3), 725–734. https://doi.org/10.1016/j.nano.2017.12.002

Singh, S., & Zlotnick, A. (2003). Observed hysteresis of virus capsid disassembly is implicit in kinetic models of assembly. *Journal of Biological Chemistry*, *278*(20), 18249–18255. https://doi.org/10.1074/jbc.M211408200

Stetefeld, J., McKenna, S. A., & Patel, T. R. (2016). Dynamic light scattering: A practical guide and applications in biomedical sciences. *Biophysical Reviews*, *8*(4), 409–427. https://doi.org/10.1007/s12551-016-0218-6

Strods, A., Ose, V., Bogans, J., Cielens, I., Kalnins, G., Radovica, I., Kazaks, A., Pumpens, P., & Renhofa, R. (2015). Preparation by alkaline treatment and detailed characterisation of empty hepatitis B virus core particles for vaccine and gene therapy applications. *Scientific Reports*, *5*(1), 11639. https://doi.org/10.1038/srep11639

Tan, T. K., Rijal, P., Rahikainen, R., Keeble, A. H., Schimanski, L., Hussain, S., Harvey, R., Hayes, J., Edwards, J. C., McLean, R. K., Martini, V., Pedrera, M., Thakur, N., Conceicao, C., Dietrich, I., Shelton, H., Ludi, A., Wilsden, G., Browning, C., … Townsend, A. R. (2021). A COVID-19 vaccine candidate using SpyCatcher multimerization of the SARS-CoV-2 spike protein receptor-binding domain induces potent neutralising antibody responses. *Nature Communications*, *12*(1), 542. https://doi.org/10.1038/s41467-020-20654-7

Thomas, J. C. (1987). The determination of log normal particle size distributions by dynamic light scattering. *Journal of Colloid and Interface Science*, *117*(1), 187–192. https://doi.org/10.1016/0021-9797(87)90182-2

U.S. Department of Health and Human Services—Food and Drug Administration. (2004). *PAT—A framework for innovative pharmaceutical development, manufacuring, and quality assurance*. Guidance for Industry. https://www.fda.gov/media/71012/download

van Rosmalen, M. G. M., Li, C., Zlotnick, A., Wuite, G. J. L., & Roos, W. H. (2018). Effect of dsDNA on the assembly pathway and mechanical strength of SV40 VP1 virus-like particles. *Biophysical Journal*, *115*(9), 1656–1665. https://doi.org/10.1016/j.bpj.2018.07.044

Vicente, T., Mota, J. P. B., Peixoto, C., Alves, P. M., & Carrondo, M. J. T. (2011). Rational design and optimization of downstream processes of virus particles for biopharmaceutical applications: Current advances. *Biotechnology Advances*, *29*(6), 869–878. https://doi.org/10.1016/j.biotechadv.2011.07.004

Wasalathanthri, D. P., Feroz, H., Puri, N., Hung, J., Lane, G., Holstein, M., Chemmalil, L., Both, D., Ghose, S., Ding, J., & Li, Z. J. (2020). Real-time monitoring of quality attributes by in-line Fourier transform infrared spectroscopic sensors at ultrafiltration and diafiltration of bioprocess. *Biotechnology and Bioengineering*, *117*(12), 3766–3774. https://doi.org/10.1002/bit.27532

West, J. M., Feroz, H., Xu, X., Puri, N., Holstein, M., Ghose, S., Ding, J., & Li, Z. J. (2021). Process analytical technology for on-line monitoring of quality attributes during single-use ultrafiltration/diafiltration. *Biotechnology and Bioengineering*, *118*(6), 2293–2300. https://doi.org/10.1002/bit.27741

Wickramasinghe, S. R., Kalbfuß, B., Zimmermann, A., Thom, V., & Reichl, U. (2005). Tangential flow microfiltration and ultrafiltration for human influenza A virus concentration and purification. *Biotechnology and Bioengineering*, *92*(2), 199–208. https://doi.org/10.1002/bit.20599

Wold, S., Sjöström, M., & Eriksson, L. (2001). PLS-regression: A basic tool of chemometrics. *Chemometrics and Intelligent Laboratory Systems*, *58*(2), 109–130. https://doi.org/10.1016/S0169-7439(01)00155-1

World Health Organization. (2021). Full evidence report on the RTS,S/AS01 malaria vaccine. https://www.who.int/initiatives/malaria-vaccine-implementation-programme

Wynne, S. A., Crowther, R. A., & Leslie, A. G. W. (1999). The crystal structure of the human hepatitis B virus capsid. *Molecular Cell*, *3*(6), 771–780. https://doi.org/10.1016/S1097-2765(01)80009-5

Yang, Y., Shi, W., Abiona, O. M., Nazzari, A., Olia, A. S., Ou, L., Phung, E., Stephens, T., Tsybovsky, Y., Verardi, R., Wang, S., Werner, A., Yap, C., Ambrozak, D., Bylund, T., Liu, T., Nguyen, R., Wang, L., Zhang, B., … Kwong, P. D. (2021). Newcastle disease virus-like particles displaying prefusion-stabilized SARS-CoV-2 spikes elicit potent neutralizing responses. *Vaccines*, *9*(2), 73. https://doi.org/10.3390/vaccines9020073

Yuan, W., & Parrish, C. R. (2001). Canine parvovirus capsid assembly and differences in mammalian and insect cells. *Virology*, *279*(2), 546–557. https://doi.org/10.1006/viro.2000.0734

Zha, L., Chang, X., Zhao, H., Mohsen, M. O., Hong, L., Zhou, Y., Chen, H., Liu, X., Zhang, J., Li, D., Wu, K., Martina, B., Wang, J., Vogel, M., & Bachmann, M. F. (2021). Development of a vaccine against SARS-CoV-2 based on the receptor-binding domain displayed on virus-like particles. *Vaccines*, *9*(4), 395. https://doi.org/10.3390/vaccines9040395

Zhang, Y., Song, S., Liu, C., Wang, Y., Xian, X., He, Y., Wang, J., Liu, F., & Sun, S. (2007). Generation of chimeric HBc proteins with epitopes in E.coli: Formation of virus-like particles and a potent inducer of antigen-specific cytotoxic immune response and anti-tumor effect in vivo. *Cellular Immunology*, *247*(1), 18–27. https://doi.org/10.1016/j.cellimm.2007.07.003

Zhao, Q., Allen, M. J., Wang, Y., Wang, B., Wang, N., Shi, L., & Sitrin, R. D. (2012). Disassembly and reassembly improves morphology and thermal stability of human papillomavirus type 16 virus-like particles. *Nanomedicine: Nanotechnology, Biology, and Medicine*, *8*(7), 1182–1189. https://doi.org/10.1016/j.nano.2012.01.007

Zhao, Q., Modis, Y., High, K., Towne, V., Meng, Y., Wang, Y., Alexandroff, J., Brown, M., Carragher, B., Potter, C. S., Abraham, D., Wohlpart, D., Kosinski, M., Washabaugh, M. W., & Sitrin, R. D. (2012). Disassembly and reassembly of human papillomavirus virus-like particles produces more virion-like antibody reactivity. *Virology Journal*, *9*(1), 52. https://doi.org/10.1186/1743-422X-9-52

Zlotnick, A., Cheng, N., Conway, J. F., Booy, F. P., Steven, A. C., Stahl, S. J., & Wingfield, P. T. (1996). Dimorphism of hepatitis B virus capsids is strongly influenced by the C-terminus of the capsid protein. *Biochemistry*, *35*(23), 7412–7421. https://doi.org/10.1021/bi9604800

Zobel-Roos, S., Mouellef, M., Siemers, C., & Strube, J. (2017). Process analytical approach towards quality controlled process automation for the downstream of protein mixtures by inline concentration measurements based on ultraviolet/visible light (UV/VIS) spectral analysis. *Antibodies*, *6*(4), 24. https://doi.org/10.3390/antib6040024

SUPPORTING INFORMATION

Additional supporting information may be found in the online version of the article at the publisher's website.

How to cite this article: Hillebrandt, N., Vormittag, P., Dietrich, A., & Hubbuch, J. (2022). Process monitoring framework for cross-flow diafiltration-based virus-like particle disassembly: Tracing product properties and filtration performance. *Biotechnology and Bioengineering*, 1–17. https://doi.org/10.1002/bit.28063